

Metadynamics Simulations of Enantioselective Acylation Give Insights into the Catalytic Mechanism of *Burkholderia cepacia* Lipase

Luca Bellucci,^{*,†} Teodoro Laino,^{‡,§} Andrea Tafi,^{*,†} and Maurizio Botta[†]

Dipartimento Farmaco Chimico Tecnologico, Università degli Studi di Siena, Via Aldo Moro 2, I-53100 Siena, Italy, Physikalisch Chemisches Institut, Universität Zürich, Winterthurerstrasse 190, CH-8057 Zürich Switzerland, and IBM Zurich Research Laboratory, Säumerstrasse 4, CH-8803 Rüschlikon Switzerland

Received November 30, 2009

Abstract: The catalytic mechanism of *Burkholderia cepacia* lipase (BCL), which catalyzes the enantioselective hydrolysis of racemic esters of primary alcohols, was investigated by modeling the first stage of the enzymatic hydrolysis of (S/R)-2-methyl-3-phenyl-propanol (MPP) acetate, using molecular dynamics simulations in a mixed quantum mechanical/molecular mechanical (QM/MM) framework. The free energy surface of the enzyme acylation reaction was computed for both enantiomers. The simulations predict the existence of different reaction free energies that favor the (S)-enantiomer over the (R)-enantiomer by 5 kcal/mol. Analysis of the structural and dynamical aspects of the simulated reactions reveals an unforeseen reorganization of the catalytic triad in the (R)-MPP ester, driven by steric hindrance and involving the residues Asp264 and Glu289. Exploiting the different catalytic role of the above-mentioned acidic residues, we suggest a way to regulate the enantioselectivity of BCL by means of a few judicious point mutations that prevent the formation of the second catalytic triad used in the reaction with the (R)-enantiomer.

1. Introduction

Serine hydrolases are one of the largest and most diverse families of enzymes in higher eukaryotes. They comprise approximately 1% of the genes in the human genome, and because of their extensive usage in organic synthesis, they are the most investigated enzymes in pharmaceutical research.

Well-known members of this enzyme family include serine proteases such as α -chymotrypsin,^{1,2} one of the first proteases to be revealed using X-ray crystallography,³ esterases such as the acetylcholinesterase enzyme⁴ (AChE), which plays an important role in Alzheimer's disease,^{5,6} and last but not least, lipases,⁷ which are widely used for biotechnological applications.^{8–12}

Although the natural function of lipases is to catalyze the hydrolysis of triacylglycerols, they also show high catalytic activity and unusual enantioselectivity toward a wide range of unnatural substrates.^{13,14} These enzymes are widely used to separate racemic mixtures of chiral esters through hydrolysis or transesterification reactions, so that enantiomeric discrimination by lipases represents one of the most efficient biocatalytic strategies for producing enantiomerically pure pharmaceutical building blocks.^{15–18}

Lipases share a characteristic catalytic mechanism with the remainder of serine hydrolases, involving the so-called catalytic triad consisting of the amino acids serine, histidine, and aspartic (or glutamic) acid. In addition to the catalytic triad, another important component of the active center of lipases is the oxyanion hole, a structural feature composed of hydrogen bond donors in the vicinity of the catalytic serine.^{1,7,19,20}

Lipases work through a general mechanism peculiar to serine proteases,^{1,7,20} known as the bi-bi ping-pong mecha-

* Corresponding author e-mail: bellucci14@unisi.it (L.B.); tafi@unisi.it (A.T.).

† Università degli Studi di Siena.

‡ Universität Zürich.

§ IBM Zurich Research Laboratory.

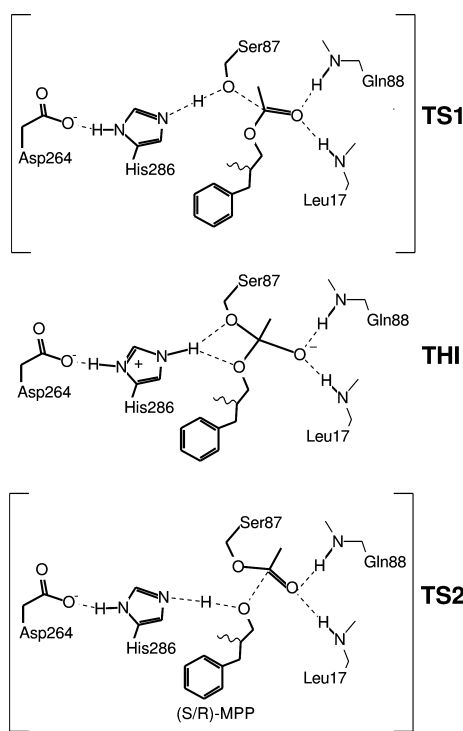


Figure 1. Proposed scheme for the acylation mechanism of *Burkholderia cepacia* lipase by acetic esters of primary alcohols. Only the main elements of the catalytic triad (Ser87, His286, Asp264), the oxyanion hole (NH of main chain Leu17 and Gln88), and the (R/S)-2-methyl-3-phenylpropyl (MPP) acetate ester are shown.

nism²⁰ and outlined by two consecutive stages: an enzyme acylation and a subsequent deacylation. The steps of acylation are summarized in Figure 1 for the case of *Burkholderia cepacia* lipase (BCL). A nucleophilic attack by the catalytic serine (Ser87) on the carbonyl carbon of an ester molecule leads to the formation of an acyl-enzyme adduct. Concurrently, the alcohol moiety is released via a negatively charged tetrahedral intermediate (THI)^{1,7} involving the substrate.

Two transition states mark the two steps of the acylation reaction (see Figure 1): TS1, regulated by the nucleophilic attack by Ser87 and by the ability of a nitrogen atom (N_e) of the catalytic histidine (His286) to accept the proton from the serine. TS2, in which the proton is transferred from His286 to the substrate, with the formation of the acyl-enzyme.

Although the catalytic roles of serine and histidine residues are unanimously accepted, a wide variety of mechanisms have been proposed to explain the role of the acidic catalytic residues (Asp264 in the case of BCL) such as the single proton-transfer mechanism,^{21–23} also supported by theoretical studies,^{24,25} the double proton-transfer, also known as the “charge-relay” mechanism,^{26,27} and the “low-barrier hydrogen bond”²⁸ and “short ionic hydrogen bond” mechanisms.²⁹

A fundamental role in the formation and stabilization of THI is played by the oxyanion hole (formed by Gln88 and Leu17 in the case of BCL), which stabilizes the negatively charged species through hydrogen bonds. It is interesting to note that, while the THI often cannot be detected with the usual substrates,^{1,30} recent studies have unambiguously

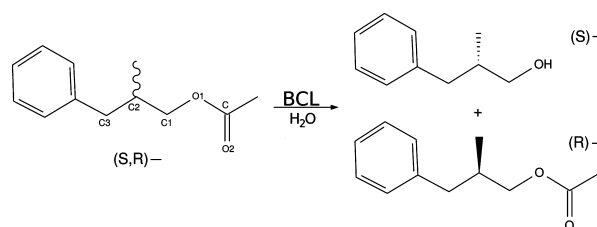


Figure 2. Hydrolysis reaction of (S)-MPP acetate catalyzed by *Burkholderia cepacia* lipase.

Table 1. Enantioselectivity (E) and Available Kinetic Constants for BCL-Catalyzed Hydrolysis of (R)- and (S)-MPP Esters

substrate	E^a	k_{cat} (min ⁻¹)	K_M (mM)
(S)-MPP acetate ³⁷	16 ± n.d.	4.7 ± 2.1	28 ± 1
(R)-MPP acetate		3.2 ± 0.4	300 ± 140
(S)-MPP butanoate ³⁵	130 ± 30		
(R)-MPP butanoate			
(S)-MPP heptanoate ³⁸	≥190 ± 30	0.4 ± 0.1	4 ± 1
(R)-MPP heptanoate		0.004 ± 0.001	3 ± 1

^a Enantioselectivity $E = (k_{\text{cat}}/K_M)_S/(k_{\text{cat}}/K_M)_R$.

shown that it is a shallow local minimum, not exceeding 3 kcal/mol in most cases.^{31,32}

The deacylation stage of the catalytic reaction, not considered in this study, proceeds via the nucleophilic addition of a lytic species (water or alcohol) to the carbonyl carbon of the acyl-enzyme. A subsequent proton transfer from the lytic species to the histidine residue³³ leads to the formation of the final product and restores the catalytic activity of the lipase.

Although all lipases exhibit enantioselectivity toward esters of secondary alcohols, *Burkholderia cepacia* lipase (BCL), formerly known as *Pseudomonas cepacia* lipase (PCL), is also able to react enantioselectively with several esters of primary alcohols.^{14,34,35} In particular, BCL catalyzes the enantioselective hydrolysis of some esters of 2-methyl-3-phenyl-propanol (MPP), which is an important precursor in pharmaceutical synthesis (see Figure 2 and Table 1).^{17,18} The experimental data shown in Table 1 underline that in these reactions BCL favors the (S)-enantiomers with varying enantioselectivity (E) values.^{35–38}

The experimental data reported in Table 1 reveal that BCL enantioselectivity toward MPP esters is mainly determined by the chirality of the substrates’ alcohol moiety: (S)-enantiomers are hydrolyzed faster than (R)-enantiomers. The acyl chain length comes into play as a modulating parameter, which strongly influences the measured kinetic values.

In the case of acetate, for instance, the enantioselectivity value is unambiguously due to the difference between the K_M constants for the (S)- and (R)-enantiomers. This suggests small differences in binding strength are at the origin of the pristine enzyme enantioselectivity for short acyl chain lengths.

For the heptanoate case, the similar K_M values entail that there are no major differences in the binding strength, therefore pinpointing the enantioselectivity of BCL for this substrate to the large difference in the k_{cat} values.

In the case of butanoate, finally, there is a substantial lack of kinetic data. However, the E value, similar in magnitude

to the one of the heptanoate ester, endorses the conjecture that the butanoate kinetic data might show a similar trend to that of the heptanoate data.

Because of the industrial relevance of MPP, numerous experimental and theoretical studies have been performed to explain and improve the enantioselectivity of BCL toward racemic esters of this substrate.^{34–44}

In particular, Mezzetti et al.³⁸ have recently resolved the X-ray structures of two phosphonate transition-state analogs of MPP heptanoate (hexylphosphonic acid (R/S)-2-methyl-3-phenylpropyl ester) bound to BCL, which contain the (R)- and (S)-enantiomers of the alcohol. In the two structures, the analogs bound to BCL in a similar manner, with the phenyl group of the alcohol pointing toward the solvent. The enantiomers adopt a so-called “mirror-image orientation” in which the methyl substituent (−CH₃), the large substituent (Phe−CH₂−) at the alcohol stereocenter, and the oxygen atom of the alcohol moiety (−O1−) are accommodated in “a similar position” in their respective complexes. As a consequence of this accommodation, due to stereochemistry requirements, the only hydrogen at the stereocenter has to “point in opposite directions”.³⁸ In the discussion of their data,³⁸ Mezzetti et al. first remark that the relative orientations of the enantiomers in the X-ray structures differ significantly from all the predictions by previous modeling studies, focused on the simulation of enantiomer recognition.^{37,39,41,43} Afterward, they try to rationalize what they call “an inconsistency”: the existence of almost superposable bound phosphonate structures, mimicking the (R)- and (S)-tetrahedral intermediates having “a similar K_M value [...] but 100-fold different k_{cat} values” in favor of the (S)-enantiomer. Mezzetti et al. hypothesize, that BCL enantioselectivity, instead of stemming from a discrimination in the transition state, might rely on the possibility of the slow (R)-enantiomer binding to the enzyme in both a *productive* and a *nonproductive* way. Only productive binding would lead to catalysis. The fast (S)-enantiomer, on the other hand, is supposed to bind only in a productive way. However, while the authors propose this explanation for the enantioselectivity of BCL, they also notice that other possibilities, such as the lack of key interactions of the (R)-enantiomer within the active site of the enzyme, cannot be excluded a priori as possible explanations for the different observed enantioselectivity. Mezzetti et al. conclude their discussion stating that “given the subtlety of the interactions, it may be difficult to rationally predict substrate modifications or lipase mutations that would increase the enantioselectivity”.

According to the insights from all the above-mentioned studies, the detailed mechanism and dynamics of the enantioselective biocatalysis by BCL is still an open question. Assessing the relative importance of chirality and acyl chain length in determining the experimental differences shown in Table 1 would certainly be an outstanding goal. Nonetheless, the complexity of the catalytic data is such that only a systematic study may result in a clear rationalization of k_{cat} and K_M values. Recently, it has been underlined that attempts to estimate small K_M differences with state of the art molecular dynamics based approaches might be unsuccessful,⁴⁵ consistent with the previous molecular modeling studies

that failed in determining the relative orientations of enantiomers into the BCL active site.^{37,39,41,43} Instead, molecular dynamics simulations have proven to be successful in many cases of k_{cat} prediction/rationalization.⁴⁵

Driven by these motivations, it seemed critical to us facing the investigation of the catalytic mechanism of BCL toward primary alcohols, keeping the effect of the acyl chain length on enantioselectivity out. Accordingly, we simulated the acylation reaction of BCL on both enantiomers of MPP acetate by performing molecular dynamics (MD) simulations using a mixed quantum mechanical/molecular mechanical (QM/MM) approach. In particular, the free energy surfaces of the acylation reaction were reconstructed for both enantiomers using the metadynamics method,^{46,47} allowing simultaneous analysis of the dynamical and structural aspects of the catalytic process during the 90 ps of MD performed for each enantiomer.

In this study, we observed that the reaction for (S)-MPP acetate proceeds in the expected way (see Figure 1), whereas the (R)-MPP substrate undergoes the reaction through a peculiar rearrangement of the active site: due to steric hindrance, the (R)-enantiomer induces a conformational change in the catalytic site, reorganizing a new triad (Ser87, His286, Glu289) instead of the native one (Ser87, His286, Asp264). As a consequence of the different reaction mechanisms, the two enantiomers show similar activation free energies ($\Delta G_S^\ddagger = 20.5 \pm 2$ kcal/mol for (S)-MPP and $\Delta G_R^\ddagger = 17.3 \pm 2$ kcal/mol for (R)-MPP) and consequently similar k_{cat} values. The MPP acetate enantiomers are therefore discriminated only at the level of the binding strength, since both enantiomers can then find similar energetically favorable reaction pathways.

On the contrary, a comparative analysis of our results with the experimental X-ray investigations on transition state analogs of heptanoate suggests that both enantiomers of that substrate have to follow an identical reaction pathway. The bulky acyl chain of heptanoate is expected to prevent the Val266 movement necessary for the His286 flip rotation. Without histidine reorganization, the enzyme is forced to work in the native form, destabilizing the acylation reaction for the (R)-enantiomer. This destabilization, due to steric hindrance, might be the source of the large difference between the kinetic constants k_{cat} for (R)- and (S)-MPP heptanoate.

2. Methods and Computational Details

2.1. System Setup. System setup and classical MD were performed with the NAMD (v.2.6)⁴⁸ and VMD (v.1.8.6)⁴⁹ software packages. The standard AMBER⁵⁰ forcefield was used for the protein, ligands, and counterions. The water was modeled using the TIP3P⁵¹ forcefield. Atom types as well as bonded and nonbonded parameters were assigned to atoms by analogy or through interpolation from those already present in the forcefield. To calculate partial atomic charges, an “elongate” conformation of (S)-MPP acetate was optimized using the *ab initio* quantum chemistry program GAMESS⁵² at the HF/6-31G* level of theory. Consequently, a set of atom-centered charges were obtained by applying

the ESP methodology as implemented in the ELPOT and PDC modules of GAMESS. Charges on equivalent atoms were equalized by averaging. The same charge values were used for the (R)-MPP acetate.

The initial substrate conformations were derived from the phosphonate inhibitor (hexylphosphonic acid (R/S)-2-methyl-3-phenylpropyl) of the BCL X-ray structure deposited in the Protein Data Bank (PDB) with accession code 1YS1 and 1YS2 for the (R)-MPP and the (S)-MPP enantiomers, respectively. The substrates were then superimposed on the isomorphous crystal structure of the activated form of the BCL⁵³ (PDB code 3LIP). The hexyl chain of the phosphonate esters was replaced by a methyl group, and the phosphorus atom was replaced by a carbon atom. Hydrogen atoms were added to the system using the VMD tools. Histidines were uncharged and protonated according the most plausible hydrogen-bonding pattern in the structure. Aspartic and glutamic acids were negatively charged, and arginines and lysines were positively charged. A geometry relaxation of the substrate molecules and catalytic residues with the rest of protein heavy atoms fixed to the crystallographic positions and without water was performed with 5000 steps of conjugate gradient geometry optimization through a NAMD minimization tool.

Each complex was then surrounded by a periodic box of TIP3P⁵¹ water molecules, and 4 Na⁺ ions were added using the VMD tools,⁴⁹ to guarantee neutrality. The same spatial arrangement of ions was adopted for both systems, placing the ions at a distance greater than 25 Å from the catalytic serine to minimize the charge effect. The total number of water molecules was 7094 in an initial rectangular box with dimensions of 63 × 70 × 62 Å.

The simulations were conducted using periodic boundary conditions and the long-range part of the electrostatics was treated with the Particle-Mesh-Ewald (PME) method,⁵⁴ with a grid size of 64 × 70 × 62. The cutoff distance for nonbonded interactions was set to 11 Å, and a switch function was applied to smooth interactions between 10 and 11 Å. The scaling factor used in NAMD for 1–4 intramolecular Coulomb interactions was set to 0.8333, which is the inverse of the standard scaling factor value used in the input AMBER file (SCEE = 1.2). The r-RESPA multiple time step method⁵⁵ was employed with 1 fs for bonded, 2 fs for the short-range part of the nonbonded, and 4 fs for the long-range part of the electrostatic forces.⁴⁸

All simulations were conducted in the NPT ensemble. The temperature was set to 300 K and controlled via Langevin thermostat.⁵⁶ The pressure was set to 1 atm and controlled via isotropic Langevin piston manostat.⁵⁷

The systems were submitted to 600 ps of MD simulation. During the first 200 ps, the proteins' heavy atoms and Na⁺ ions were harmonically restrained with a force constant of 10 kcal/(mol Å²). Subsequently, 200 ps of dynamics were performed with the force constant set to 5 kcal/(mol Å²), and finally 200 ps with the force constant set to 1 kcal/(mol Å²). This allowed the equilibration of the solvent and the proper readjustment of the cell volume without disruption of the ligand conformation, or of the lipase structure that preserved the active open form.⁷ The final structures were

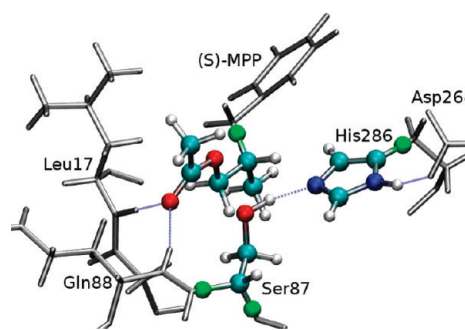


Figure 3. Main residues of the catalytic site and (S)-MPP acetate substrate. The atoms comprising the QM region that were used in this study are shown in ball-and-stick representation. The link hydrogen atoms are highlighted in green; the MM region, in gray, is shown in tube representation.

then used as starting point for QM/MM simulations. To ensure the validity of the structures obtained, a subsequent run was continued for a further 100 ps without restraints and with velocities redistributed according to a Boltzmann distribution. The mean values of the protein heavy atoms RMSD calculated with respect to the initial conformation were 0.87 and 0.92 Å for the (R)-MPP and (S)-MPP systems, respectively (RMSD time evolutions are available in the Supporting Information).

2.2. QM/MM System. In order to obtain an accurate description of the chemical processes involved in the reaction mechanism while reducing the computational cost inherent in *ab initio* calculations, a QM/MM scheme was chosen to model the reactive site.

The QM/MM driver^{58,59} is based on the QM program QUICKSTEP^{60,61} and the MM driver FIST, which are both part of the freely available CP2K package.⁶² The quantum part is treated at the density functional theory (DFT) level. This region consists of the substrate, with the exception of the large substituent (Phe–CH₂–), the Ser87 side chain with inclusion of the C_α backbone atom (at a two atoms distance from the attacking oxygen), and the imidazole ring of His286, adding up to a total number of 35 atoms. This set contains all the atoms directly involved in the reaction or whose stabilization of the reaction intermediates cannot be described uniquely with electrostatic effects. Therefore, the only atoms which have been excluded from the quantum region are the hydrogens of the oxyanion hole and side chain of Asp264 and Glu289 near the His286. The exclusion of these atoms from the quantum region is not crucial due to the evidence^{24,25,33,63} that they have mainly an electrostatic stabilization role.

The boundary between the QM and the MM regions (C_γ–C_β of His286, C_α–CO and C_α–NH of Ser87, and C₂–C₃ of MPP) were saturated by link hydrogen atoms (see Figure 3). In agreement with the IMOMM link scheme,⁶⁴ the scaling factor projecting the forces on the capping hydrogen was refined to maintain the QM/MM bond distances at the same values of the forcefield.

The remaining part of the system, including the water molecules and counterions, has been modeled at the classical level with the AMBER forcefield, explicitly taking into account the steric and electrostatic effects of the substrate, the enzyme, and the solvent.

A triple- ζ valence basis set with two sets of polarization functions, TZV2P,⁶⁵ and an auxiliary plane-wave basis set with a density cutoff of 280 Ry were used to describe the wave function and the electronic density. Dual space pseudopotentials^{66,67} were used for describing core electrons and nuclei. We used the gradient-corrected Becke exchange⁶⁸ and the Lee, Parr, and Yang correlation functional (BLYP).⁶⁹ Energies were tested for convergence with respect to the wave function gradient (5×10^{-7} Hartree) and cell size, which was required to be no smaller than 16.0 Å (cubic box) to achieve a correct decoupling between the periodic images.⁷⁰

The QM regions were first minimized by keeping the entire MM subsystem frozen. Subsequently, a complete minimization was performed over the entire system, employing a conjugate gradient method as implemented in CP2K. Root-mean-square (RMS) values of 0.005 hartree·Bohr⁻¹ for force and 0.005 Bohr for positions were selected as convergence criteria. The systems were then subject to a brief equilibration by means of a QM/MM MD simulation in the NVT ensemble for 2.5 ps. The temperature was set to 300 K, and each degree of freedom was controlled via a Nosé–Hoover thermostat^{71,72} with a time constant of 50 fs. A single integration time step of 0.50 fs was used.

2.3. Metadynamics. The choice of collective variables (CV) is crucial in metadynamics^{46,47} for its successful application. Looking at Figure 1, the fundamental geometrical variables describing the acylation reaction can be identified as the distances between the atoms involved in the nucleophilic attack, the subsequent release of the alcohol's moiety, and the hydrogen transfer.

During the nucleophilic attack, the $r_{\text{C}-\text{O}}$ variable, defined as the distance between the carbonyl carbon atom of the ester group and the serine oxygen atom, gradually decreases until the formation of the acyl-enzyme complex. In contrast, the $r_{\text{C}-\text{O}1}$ variable, defined as the distance between the carbonyl carbon atom of the ester and the alcohol oxygen atom, gradually increases during the nucleophilic attack and the subsequent release of the alcohol moiety. The variable $r_{\text{H}-\text{N}_e}$, defined as the distance between the serine hydrogen and the histidine nitrogen, traces the proton transfer that occurs during the reaction.

To reduce the complexity while maintaining an accurate description of the system, 2 CVs were chosen from the three variables mentioned and defined as $\text{CV}_a(r) = r_{\text{H}-\text{N}_e}$ and $\text{CV}_b(r) = (r_{\text{C}-\text{O}1} - r_{\text{C}-\text{O}})$, the difference between the bond distances $r_{\text{C}-\text{O}1}$ and $r_{\text{C}-\text{O}}$, spanning a two-dimensional subspace of the free energy surface reaction. The metadynamics runs were performed using Gaussian-shaped potential hills with a height of 3.0×10^{-3} Hartree and a width of 0.1 Bohr.

The hills were spawned at intervals of 20 fs of QM/MM MD. To restrict the surface of exploration, an upper limit in the $\text{CV}_a(r)$ was imposed with activation of a quadratic wall positioned at 2.20 Å, with a quadratic potential constant of 30.0 kcal/(mol Å²), whereas $\text{CV}_b(r)$ was delimited by two quadratic walls positioned at -1.5 and 1.5 Å, with a quadratic potential constant of 20.0 kcal/(mol Å²). QM/MM metadynamics were conducted in the NVT ensemble. The temper-

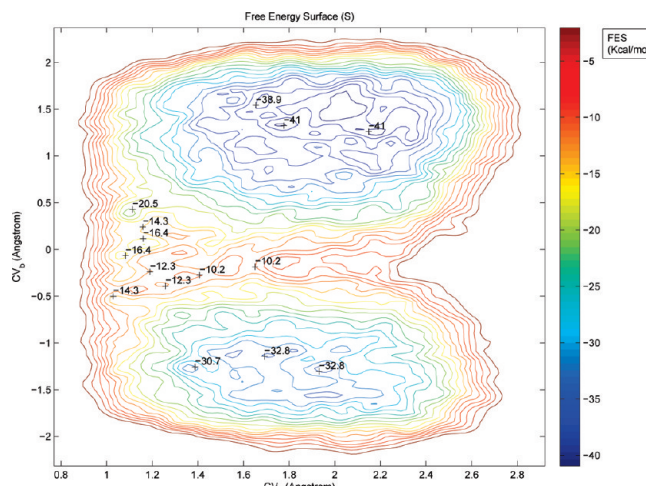


Figure 4. Acylation reaction free energy surface of the (S)-MPP system reconstructed using metadynamics as a function of two CVs, specifically, $\text{CV}_a(r) = r_{\text{H}-\text{N}_e}$ and $\text{CV}_b(r) = (r_{\text{C}-\text{O}1} - r_{\text{C}-\text{O}})$. Energy is in kcal/mol; the CV values are expressed in Å.

ature was set to 300 K, and each degree of freedom was controlled via a Nosé–Hoover thermostat^{71,72} with a time constant of 50 fs. Temperature stability was monitored along the metadynamics runs (see the Supporting Information). A single integration time step of 0.5 fs was used. The runs were protracted for about 90 ps for both systems until they showed a free diffusivity along the CVs. These convergence criteria were chosen in agreement with the guidelines published in a recent paper directed to assess the accuracy of metadynamics.⁷³ Trajectories were saved every 20 steps (10 fs time interval) of metadynamics for subsequent analysis. The long QM/MM MD simulation times guaranteed an extensive sampling of the configurational space, important for providing meaningful determination of the energetics for enzymatic reactions.⁷⁴

3. Results

To elucidate catalytic mechanism of BCL at the molecular level, we reconstructed the free energy surfaces (FESs) for the enzyme acylation reaction by MPP acetate enantiomers according to two defined CVs, $\text{CV}_a(r) = r_{\text{H}-\text{N}_e}$ and $\text{CV}_b(r) = (r_{\text{C}-\text{O}1} - r_{\text{C}-\text{O}})$, using metadynamics and a QM/MM computational framework.

The results of our calculations are given in Figures 4 and 5 for (S)-MPP acetate and (R)-MPP acetate, respectively. The two FESs show similar contours, and in both cases, two broad minima can be recognized corresponding to the enzyme–substrate complex (ES) and to the enzyme–product complex (EP). The ES region spans from 0.75 to 2.5 Å for $\text{CV}_a(r)$ and negative values for $\text{CV}_b(r)$. The EP region corresponds to values from 0.75 to 2.5 Å for $\text{CV}_a(r)$ and positive values for $\text{CV}_b(r)$.

In Figure 6, the time evolution of $\text{CV}_b(r)$ is displayed together with the times at which the acylation reaction and the reverse reaction have occurred. The observation of the “retro” reaction restoring the reagent species highlights the early achievement of free diffusivity conditions along the CVs. According to the description of the reaction profile,

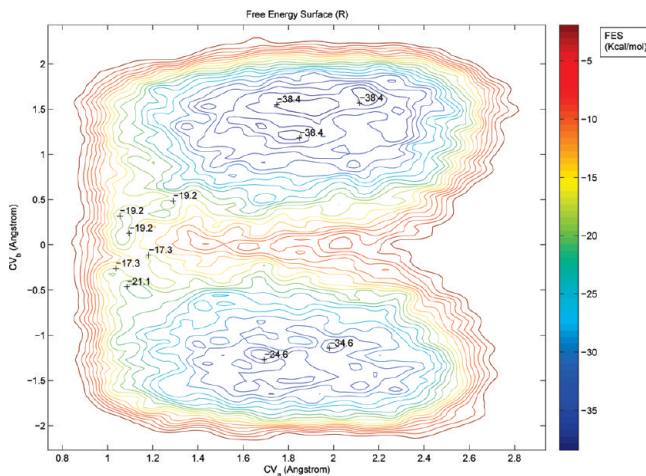


Figure 5. Acylation reaction free energy surface of the (R)-MPP system reconstructed using metadynamics as a function of two CVs, specifically, $CV_a(r) = r_{H-N}$, and $CV_b(r) = (r_{C-O_1} - r_{C-O})$. Energy is in kcal/mol; the CV values are expressed in Å.

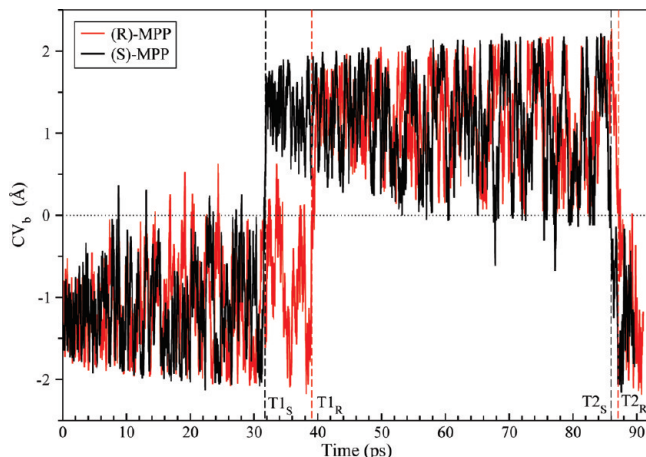


Figure 6. Time evolution of $CV_b(r)$ during the metadynamics run. The trend of the $CV_b(r)$ for (R)-MPP is shown in red, whereas the trend of the $CV_b(r)$ for (S)-MPP is given in black. Vertical lines give the time at which the reaction takes place. The labels $T1_S$ and $T1_R$ refer to the acylation reaction for the (S)- and (R)-enantiomers, respectively. $T2_S$ and $T2_R$ refer to the reverse reaction.

it can be observed that the reaction occurs after 32 ps in the case of the (S)-enantiomer and after 39 ps in the case of the (R)-enantiomer, that is, when $CV_b(r)$ changes from negative to positive values.

Both acylation reactions are exothermic, and the total free energy changes, extrapolated from the values reported in Figures 4 and 5, are about $\Delta G = -8 \pm 2$ kcal/mol for (S)-MPP and $\Delta G = -3 \pm 2$ kcal/mol for (R)-MPP. As proposed in Figure 1, both reactions proceed from the ES complex to the TS1 species through nucleophilic attack and proton transfer. The TS1 structures for both enantiomers can be localized on the FES near a value of 1.3 Å for $CV_a(r)$ and -0.5 to 0.0 Å for $CV_b(r)$.

In the case of (S)-MPP acetate, the acylation reaction proceeds from TS1 to the proposed THI: in Figure 4, near a value of about 0 Å for $CV_b(r)$ and about 1.1 Å for $CV_a(r)$,

it is possible to identify a shallow basin which reflects the presence of a transient species, possibly to be identified as the THI. The resolution of the metadynamics run, however, proportional to the height of the Gaussian functions (3.0×10^{-3} Hartree), is of about the same magnitude as the observed stabilization energy for the supposed THI local minimum. Due to this remark and since detailed inspection of trajectories did not succeed in identifying a proper geometrical characterization of the supposed THI, one cannot discard the possibility that such a minimum is only an aberration due to metadynamics. Finally, after the shallow basin, the reaction goes toward the presumed TS2, with the consecutive release of the (S)-alcohol.

In the case of (R)-MPP, the FES region corresponding to TS1, THI, and TS2 is extremely flat, and the tetrahedral intermediate is not as readily identifiable (see Figure 5) as in the (S)-MPP case. In the EP basin, the reaction proceeds toward the release of the alcohol moiety in a similar way as it does with (S)-MPP.

Although Figures 4 and 5 display some differences in the contours of the FESs, notably in the EP basin, both surfaces exhibit extremely similar topological features. A quantitative analysis reveals that the free energy barrier in going from the ES basin to the first transition state (TS1) is $\Delta G_S^{\ddagger} = 20.5 \pm 2$ kcal/mol for (S)-MPP and $\Delta G_R^{\ddagger} = 17.3 \pm 2$ kcal/mol for (R)-MPP. The reverse reaction (from the EP basin to the transition state TS2) occurs with a free energy barrier of about 29 ± 2 and 21 ± 2 kcal/mol for (S)-MPP and (R)-MPP, respectively. As a whole, the difference in the total free energy change for the MPP acetate ester is $\Delta\Delta G_{S-R} = -5 \pm 2$ kcal/mol in favor of the release of the (S)-MPP alcohol moiety.

The large magnitude of the barriers involved in the forward and backward reaction paths addresses both enantioselective hydrolyses of the acetate esters as thermodynamically controlled reactions. In fact, at least for the (R)-enantiomer, the barriers of both forward and backward reactions are comparable, within computational errors. This casts serious doubts on the possibility to rationalize quantitatively the data reported in Table 1 simply applying the conventional Michaelis–Menten mechanism, which correlates the kinetic constant k_{cat} to the forward reaction only and assumes the acylation step to be irreversible.⁷⁵ Therefore, the atomistic aspects involved in the acylation reaction were analyzed to properly understand the significance of kinetic and calculated thermodynamic data.

To investigate the reaction mechanism, some geometrical variables describing the motion of the catalytic triad along the metadynamics trajectory were monitored. In particular, the dihedral angles χ_1 (along the $C_{\alpha}-C_{\beta}$ bond) and χ_2 (along the $C_{\beta}-C_{\gamma}$ bond) describe the dynamic behavior of the imidazole ring of His286 during the reaction. Their time evolution is reported in Figures 7 and 8, respectively.

In the case of the (S)-MPP acetate, the time evolution of χ_1 values shows a step at about 30 ps corresponding to a main movement (see Figure 7). This can be described as a sort of “pivoting” motion of the His286 imidazole ring, which drives the hydrogen proton transfer from the Ser87 residue

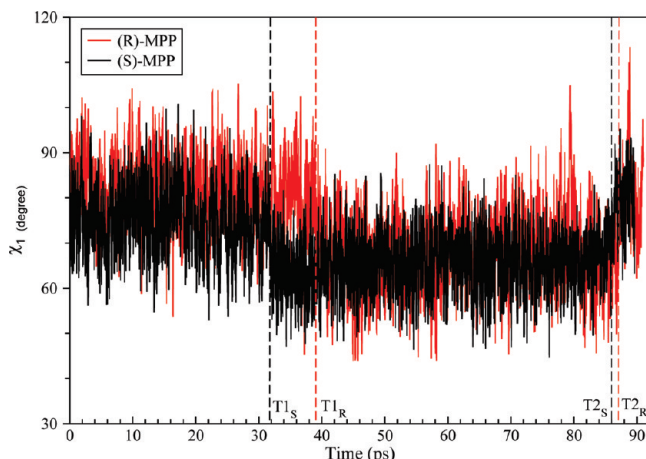


Figure 7. Time evolution of the χ_1 dihedral angle along the $C_\alpha-C_\beta$ bond of His286 during the metadynamics run. Red shows the course of χ_1 for (R)-MPP, black that of χ_1 for (S)-MPP. Vertical lines indicate the time at which the reaction takes place, as described in the caption of Figure 6.

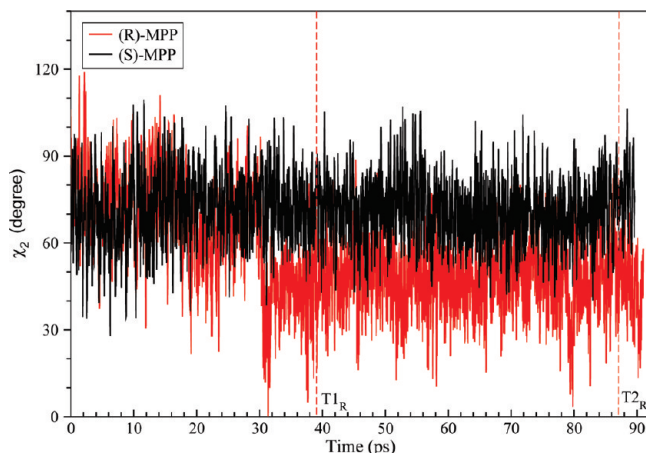


Figure 8. Time evolution of the χ_2 dihedral angle along the $C_\beta-C_\gamma$ bond of His286 during the metadynamics run. Red depicts the course of χ_2 for (R)-MPP, black that of χ_2 for (S)-MPP. Vertical lines indicate the time at which the reaction takes place, as described in the caption of Figure 6.

to the oxygen atom of the alcohol moiety. As in contrast to the dihedral angle χ_1 , the time evolution of the dihedral angle χ_2 , displayed in Figure 8, reveals only fluctuations of the imidazole ring plane.

Figure 9 displays the superposition of representative snapshots of the metadynamics trajectory of (S)-MPP acetate. The structures identify a progression from an initial to a final reaction state passing through an “intermediate” species. As shown in Figure 9, the $-CH_2-$ group of the large substituent of the (S)-MPP enantiomer points toward Leu17. This avoids any steric hindrance between His286 and the alcohol moiety, allowing the pivoting of His286 and the reaction to occur smoothly.

In the case of the (R)-MPP acetate, the time evolution of the χ_1 values shows a similar trend with respect to (S)-MPP, while a peculiar rotation of about $30\text{--}40^\circ$ of the χ_2 dihedral angle is observed (red in Figure 8), which occurs at about 30 ps, that is, 10 ps before the reaction takes place. The motion corresponds to a rotation or “flip” of the imidazole

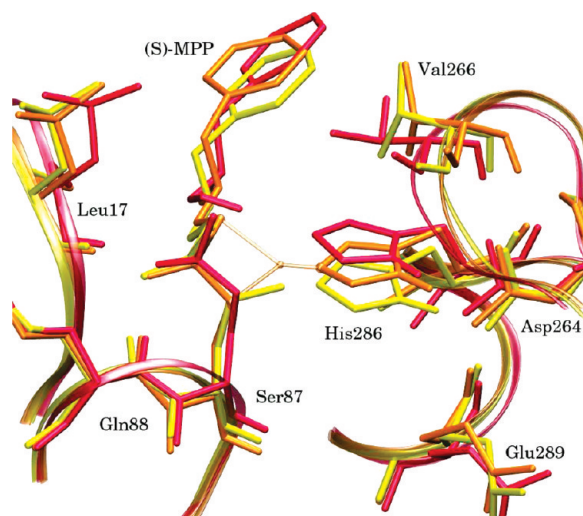


Figure 9. Superposition of representative snapshots of the metadynamics trajectory showing the evolution of the positions of the catalytic triad during the acylation reaction for (S)-MPP ester. The color code (yellow \rightarrow orange \rightarrow red) corresponds to structures at 31.57, 31.72, and 54.43 ps of simulation, respectively.

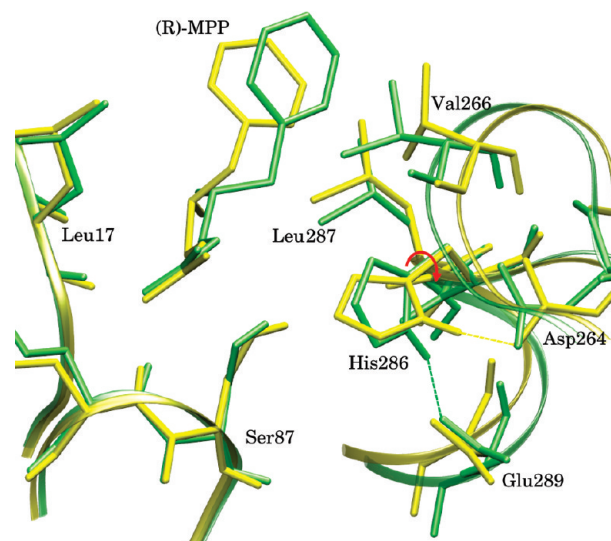


Figure 10. Catalytic triad residues. (R)-MPP ester enantiomer and main residues surrounding the catalytic triad are displayed in stick representation. Only polar hydrogens are shown. A representative snapshot of the initial conformation is depicted in yellow. A representative snapshot of the metadynamics run (40 ps) after rotation of the catalytic histidine is depicted in green. The hydrogen bond between His286 and Glu289 is depicted as a dashed green line, while the hydrogen bond between His286 and Asp264 is depicted as a dashed yellow line. The χ_2 dihedral angle is depicted as a red arrow.

ring. In Figure 10, the superposition of two representative structures extracted from metadynamics runs, sampling the catalytic environment before and after the histidine flip, is shown. From the two snapshots of Figure 10, we can reconstruct the His286 rearrangement path, which is induced by the mechanical effect of a clash between the (R)-alcohol moiety and the imidazole ring. Interesting enough, it is possible to observe that, after the flip has occurred, the alcohol moiety can get closer to the catalytic triad, with a

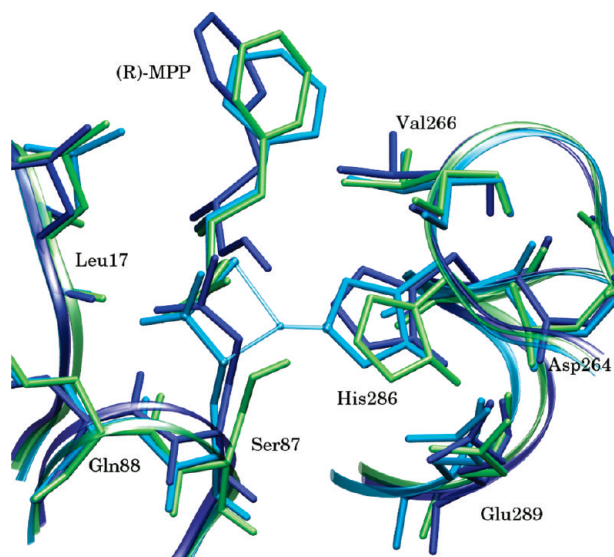


Figure 11. Superposition of representative snapshots of the metadynamics trajectory showing the evolution of the positions of the catalytic triad during the acylation reaction for (R)-MPP ester. The color code (green → cyan → blue) corresponds to structures at 35.34, 39.65, and 67.69 ps of simulation, respectively. The progression is shown from an initial to a final reaction state passing through an “intermediate” species represented by a selected snapshot of the metadynamics trajectory during the hydrogen transfer process. Even if the $-\text{CH}_2-$ group of the large substituent of the (R)-MPP enantiomer points toward His286, the reaction proceeds (after flip motion) as in the case of the (S)-enantiomer.

portion of the large substituent ($\text{Phe}-\text{CH}_2-$) inserted more deeply into a cleft formed by the side chain of Leu287 and His286, also known as the “His gap”.^{76,77} Therefore, the His286 ring rotation increases the size of the narrow “His gap” cleft, facilitating the approach of the (R)-MPP alcohol toward the catalytic triad. It is important to observe that the flip movement is permitted by a preparatory rearrangement of the side chain of Val266, which rotates by about 120° with respect to the initial position. As shown in Figure 10, after this rotation, one of the Val266 methyl groups no longer points toward the histidine imidazole, allowing for a greater mobility of this residue.

During the histidine flip, the hydrogen bond between the catalytic triad residues His286 and Asp264 breaks, and another hydrogen bond forms between the rotated His286 and Glu289 to restore an alternative catalytic triad (Ser87, His286, and Glu289). Because of the current choice of CVs, the transition state associated with the catalytic triad reorganization has not been detected, as it lays in a space orthogonal to the one we used for exploring the free energy surface. However, after such a reorganization of the catalytic triad, the acylation reaction of the (R)-enantiomer proceeds as in the case of the (S)-enantiomer and can be described with the selected CVs without a loss of accuracy. Figure 11 shows the superposition of representative snapshots of the metadynamics trajectory after the flip motion, showing the time evolution of the (R)-enantiomer and of the residues surrounding the substrate, including the alternative catalytic triad, during the reaction.

Figures 9 and 11 allow the reconstruction of a path for the acylation reaction, which is consistent with the serine protease mechanism suggested by Radisky et al.⁷⁸ and by Fuhrmann et al.,²⁹ on the basis of experimental evidence. Moreover, Figures 9 and 11 highlight the different “adaptation” of the enzymatic catalytic triad to the two enantiomers. In the (R)-MPP system, the preliminary histidine flip motion was necessary for the occurrence of the reaction; on the contrary, the acylation reaction of the (S)-MPP ester occurred without any disruption or rearrangement of the catalytic triad.

To the best of our knowledge, this is the first time that clear evidence is provided, at the atomistic level, of the possibility for BCL to shift toward a secondary catalytic triad by preliminary histidine flip motion.

It is worth noting that, as demonstrated by the computed FESs, (i) BCL retains similar catalytic activity using the secondary triad Ser87, His286, and Glu289 and (ii) the reorganization of the enzyme environment is associated with a destabilization of the acyl-enzyme adduct, which is reflected in the smaller free energy difference calculated for the acylation reaction of (R)-MPP acetate.

The flip motion has been observed because BCL contains two alternative acidic residues able to participate in the formation of the catalytic triad: Asp264 and Glu289. A closely related lipase, *Pseudomonas glumae*, exhibits the same characteristic arrangement of acidic residues, Asp263 and Glu288, equivalent to Asp264 and Glu289 of BCL.^{79,80} In that case, mutation of Asp263 into alanine yielded a lipase with 25% of the original activity.⁸¹ This experimental observation strengthens the point that, similarly to *Pseudomonas glumae*, the Glu289 residue of BCL can also serve as an alternative proton acceptor.

The different catalytic mechanisms for the (S)- and (R)-enantiomers suggest a way to increase further BCL enantioselectivity by mutation of Glu289 into an aprotic residue such as alanine. In fact, the lack of an additional donor for the formation of the secondary catalytic triad would render the standard catalytic triad the only one accessible for the conversion of the (R)-enantiomer, with a large steric hindrance. This would destabilize the reaction pathway, providing a clean way to deplete the catalytic activity for one of the two enantiomers.

Other structural adjustments of the enzyme environment can be readily observed by root mean-square deviation (RMSD) and root mean-square fluctuation (RMSF, i.e. standard deviation) values of individual side chain residues within 6 Å of the catalytic triad, calculated with respect to the starting position of the metadynamics run. RMSDs and RMSFs for selected residues, time averaged over the simulation, are reported in Figures 12 and 13 for both enantiomers.

The residues with the highest RMSD are Glu289, Phe119, and Val266. Glu289 shows a high RMSD and RMSF only in the case of the (S)-MPP because it is not involved in any hydrogen bond within the catalytic triad. The mobility of this residue, on the contrary, is reduced in the (R)-MPP system due to the hydrogen bond formation with His286 in the secondary catalytic triad. Phe119 and Val266 are adjacent residues and form part of a hydrophobic pocket, which

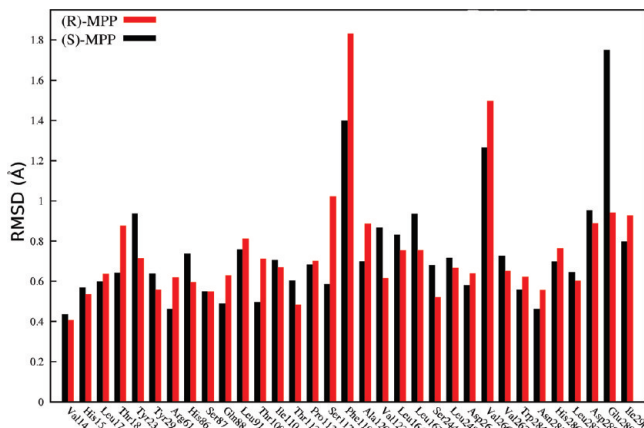


Figure 12. RMSD of residue side chain atoms. Only residues within 6 Å of the catalytic triad are reported. Red bars correspond to the (R)-MPP enantiomer; black bars correspond to the (S)-MPP enantiomer.

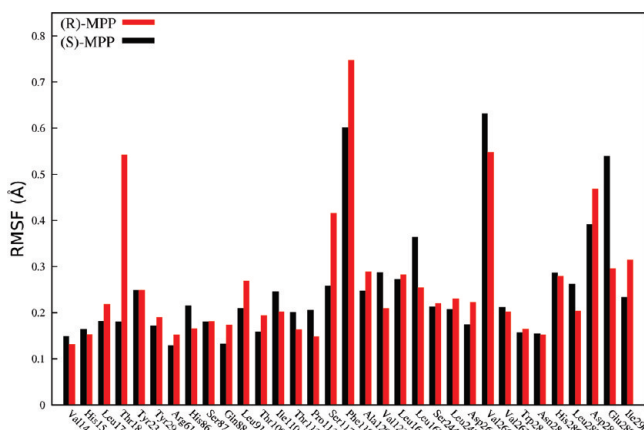


Figure 13. RMSF of residue side chain atoms. Only residues within 6 Å of the catalytic triad are reported. Red bars correspond to the (R)-MPP enantiomer; black bars correspond to the (S)-MPP enantiomer.

comprises also Pro113, Leu164, Leu167, and Val267, also known as the hydrophobic groove HA,⁸² where the acyl chain of the esters is accommodated. Accordingly, the fluctuations of the Phe119 side chain have been related to the emptiness of the HA groove usually occupied by acyl chains. The movement of the Val266 residue deserves more attention: it was monitored by following the time evolution of the dihedral angle along the C_α–C_β bond of this residue and of the distance between His286 C_{δ2} and Val266 C_β atoms (see in Figure 14A and B). In the case of the (R)-MPP system, as discussed above, a rotational rearrangement of the Val266 side chain occurs at about 20 ps (see Figure 14A), before both the His286 flip and pivoting movements. In the case of the (S)-MPP system, a comparable side chain rotation takes place as well, however, as a consequence of the reaction progress. Figure 9 shows that this rotation for the (R)-enantiomer is promoted by the pivoting movement of His286 and allows the relaxation of this residue.

An insight on the role of the acyl chain in the acylation reaction has been obtained superimposing the previously described X-ray structures of the hexylphosphonic transition-state analogues³⁸ onto the “intermediate” snapshots of the

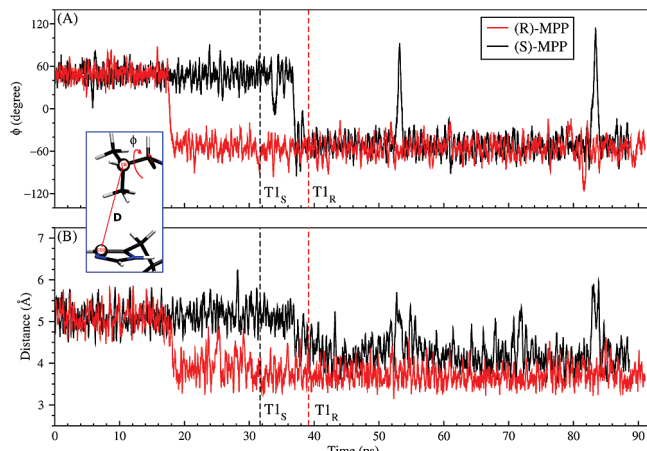


Figure 14. Time evolution of the dihedral angle along the C_α–C_β bond of Val266 (A) and of the intermolecular distance between His286 C_{δ2} and Val266 C_β atoms (B) during the metadynamics runs. The trend of the values for (R)-MPP is shown in red, whereas the trend of the values for (S)-MPP is given in black. Vertical dashed lines highlight the time at which the acylation reaction takes place. Labels T1_S and T1_R refer to the acylation reaction for the (S)- and (R)-enantiomers, respectively. In the blue box, a representative snapshot of the initial Val266 and His286 relative orientation is depicted: a red line shows the monitored distance (*D*), while a red arrow shows the monitored dihedral angle (ϕ).

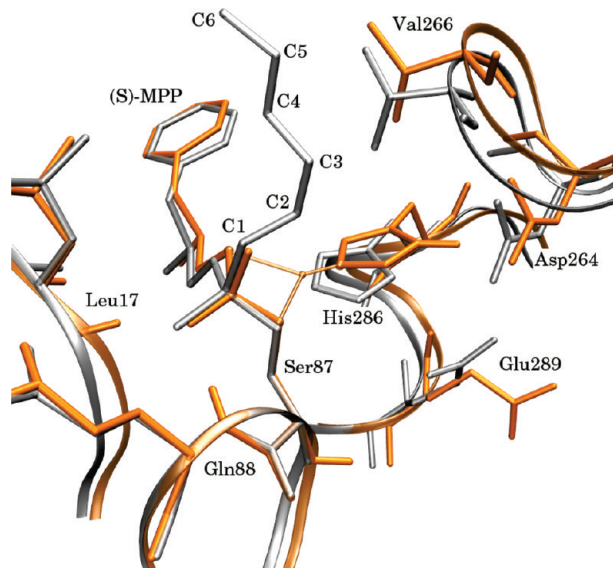


Figure 15. Superposition of a molecular dynamics snapshot of the (S)-MPP “intermediate” species (orange) on the X-ray S-enantiomer phosphonate analogue structure (white).

(S)-MPP and (R)-MPP species (Figures 15 and 16). Although comparison with transition state analogues should be used with caution,⁸³ since here the catalytic histidine is not involved in the proton transfer and the system is in a relaxed conformation, the excellent overlap displayed in the figures indirectly confirms the accuracy of our computational setup.

As shown in Figures 15 and 16, the hexyl chains of both phosphonate esters extend into the hydrophobic groove HA. Both X-ray structures exhibit a favorable interaction between Val266 and the acyl chain, mainly because one of the Val266 methyl groups points toward the catalytic His286. This

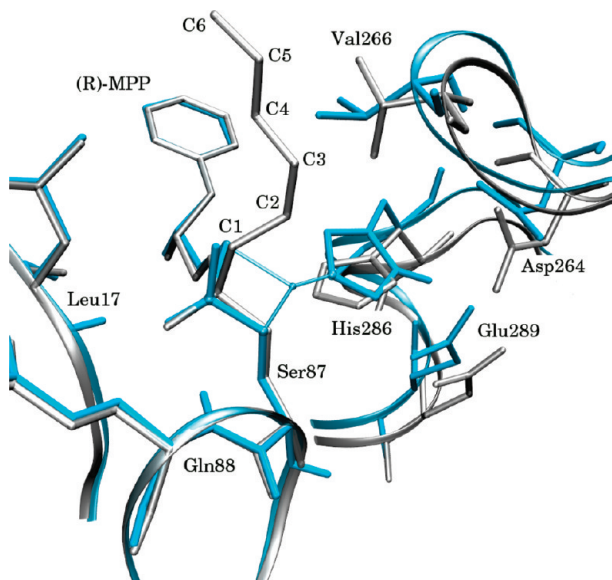


Figure 16. Superposition of a molecular dynamics snapshot of the (R)-MPP “intermediate” species (cyan) on the X-ray structure of the (R)-enantiomer phosphonate analogue (white).

peculiar arrangement is necessary to avoid a remarkable steric hindrance between the rotated Val266 and the C3–C4 positions of the phosphonate acyl chain that would arise further to a hypothetical rearrangement of the catalytic triad (see Figure 16). Therefore, by choosing the acyl chain length appropriately, the rotation of the residue Val266 can be optimally controlled or even prevented, which supports the experimental evidence reported in Table 1 that acetate exhibits a moderate enantioselectivity and heptanoate has the largest enantioselectivity, whereas butanoate shows an intermediate value.

The results of this study offer an important interpretation of the kinetic data shown in Table 1. The similar values for k_{cat} in the case of acetate compared to the different values of k_{cat} for heptanoate can be justified with the finding that, in the case of acetate, the (R)- and (S)-enantiomers follow two different reaction pathways, using two different catalytic triads. Therefore, for the acetate, the enantioselectivity originates only at the level of the binding strength, since both enantiomers can find energetically favorable reaction pathways.

On the contrary, in the case of heptanoate, the reaction pathway is identical for (R)- and (S)-enantiomers. A possible rationale is that the accommodation of an heptanoil chain in the active site of BCL prevents the Val266 side chain movement so that the His286 flip rotation is hampered and the catalytic triad of the enzyme is “forced” to work in the native form. The blocked conformation thus creates a steric hindrance between the (R)-enantiomer and His286, which destabilizes the acylation reaction. This destabilization, which is present only for the (R)-enantiomer, is the source of the large difference between the two kinetic constants k_{cat} for (S)- and (R)-MPP heptanoate.

4. Conclusion

Enantioselectivity is fundamental to the design of new and more efficient synthetic routes for modern drugs.

In this work, we report a study on the BCL-catalyzed hydrolysis of the acetic ester of (R/S)-2-methyl-3-phenylpropanol (MPP), which is an important precursor in pharmaceutical synthesis, using a QM/MM scheme based on DFT for treating the quantum region. Using metadynamics for both (S)- and (R)-enantiomers, we computed the free energy surfaces of the catalyzed reaction with respect to two collective variables that mapped the entire reaction path.

Our results show that the (R)-enantiomer cannot efficiently undergo the acylation reaction using the BCL native catalytic triad Ser87, His286, and Asp264, due to steric hindrance. This enantiomer, instead, can follow a different and fruitful reaction path exploiting an alternative triad based on Ser87, His286, and Glu289. Residue Glu289, therefore, due to its closeness to Asp264 and His286, plays a fundamental role as an alternative proton acceptor.

From our studies, we were also able to identify in residue Val266 one of the sources of the different stereospecificity shown by BCL toward substrates with different acyl chain lengths. A short acyl chain, in fact, allows mobility of Val266, which is essential to promote the flip motion of His286. On the contrary, longer acyl chains obstruct Val266 side chain rotation. A smaller mobility of this residue makes the rearrangement of His286 more difficult and, consequently, increases the stereospecificity of the catalyzed reaction.

The present work contributes, with state-of-the-art computer simulations, to the understanding of atomistic aspects of the catalytic triad in BCL when reacting with two different enantiomers of MPP and provides detailed information on how to regulate the enantioselectivity of this enzyme. In fact, we hypothesize that the mutation of Glu289 or Asp264 into an aprotic residue, or mutations designed to affect the mobility of either Val266 or the catalytic triad, would be possible strategies to regulate the stereoselectivity of the BCL lipase.

After the execution of this work, a paper concerning the control of BCL enantioselectivity by engineering the substrate accessibility channel appeared,⁸⁴ which gives experimental evidence of our theoretical insights on the essential contribution of Val266 to the enzyme enantiomeric preference. Lafaquière et al., working with (R/S)-2-chloro ethyl 2-bromophenylacetate, have in fact observed a reversal of the enantioselectivity by mutation of Val266 into a “most compact glycine”. According to our catalytic mechanism rationalization, annihilation of Val266 side chain hindrance is very much expected to affect the catalytic histidine mobility producing dramatic consequences on the enzyme enantioselectivity.

Acknowledgment. We thank the Swiss National Supercomputing Center (CSCS) for providing the computational resources used in this work on the IBM sp5 machine. L.B. gratefully acknowledges Prof. Jürg Hutter (University of Zurich Institute of Physical Chemistry) for his hospitality and the opportunity to collaborate with the CP2K development team. Project FIRB 2003 “Novel environment friendly biotransformations and optimization of industrial processes based on the use of enzymes and organometallic catalysts”, protocol number RBNE 034XSW_005, of Ministero Italiano della Università e della Ricerca, is gratefully acknowledged.

Supporting Information Available: Further details about system setup, forcefield parameters, RMSD equilibration data and metadynamics configurations are provided in the Supporting Information. This information is available free of charge via the Internet at <http://pubs.acs.org/>.

References

- (1) Hedstrom, L. *Chem. Rev.* **2002**, *102*, 4501–4523.
- (2) Norin, M.; Hult, K.; Mattson, A.; Norin, T. *Biocatal. Biotransform.* **1993**, *7*, 131–147.
- (3) Matthews, B. W.; Sigler, P. B.; Henderson, R.; Blow, D. M. *Nature* **1967**, *214*, 652–656.
- (4) Quinn, D. M. *Chem. Rev.* **1987**, *87*, 955–979.
- (5) Trinh, N. H.; Hoblyn, J.; Mohanty, S.; Yaffe, K. *J. Am. Med. Assoc.* **2003**, *289*, 210–216.
- (6) Soreq, H.; Seidman, S. *Nat. Rev. Neurosci.* **2001**, *2*, 294–302.
- (7) Schmid, R. D.; Verger, R. *Angew. Chem., Int. Ed.* **1998**, *37*, 1609–1633.
- (8) Jaeger, K. E.; Eggert, T. *Curr. Opin. Biotech.* **2002**, *13*, 390–397.
- (9) Reetz, M. T. *Curr. Opin. Chem. Biol.* **2002**, *6*, 145–150.
- (10) Guo, Z.; Xu, X. *Org. Biomol. Chem.* **2005**, *3*, 2615–2619.
- (11) Gupta, R.; Gupta, N.; Rathi, P. *Appl. Microbiol. Biotechnol.* **2004**, *64*, 763–781.
- (12) Ban, K.; Kaieda, M.; Matsumoto, T.; Kondo, A.; Fukuda, H. *Biochem. Eng. J.* **2001**, *8*, 39–43.
- (13) Botta, B.; Zappia, G.; Tafi, A.; Botta, M.; Manetti, F.; Cernia, E.; Milana, G.; Palocci, C.; Soro, S.; Monache, G. D. *J. Mol. Catal. B: Enzym.* **2002**, *16*, 241–247.
- (14) Bornscheuer, U. T.; Kazlauskas, R. J. *Hydrolases in Organic Synthesis: Regio-and Stereoselective Biotransformations*, 2nd ed.; Wiley-VCH: Weinheim, Germany, 2006.
- (15) Ghanem, A. *Tetrahedron* **2007**, *63*, 1721–1754.
- (16) Gotor-Fernández, V.; Brieva, R.; Gotor, V. *J. Mol. Catal. B: Enzym.* **2006**, *40*, 111–120.
- (17) Delinck, D. L.; Margolin, A. L. *Tetrahedron Lett.* **1990**, *31*, 6797–6798.
- (18) Stoermer, D.; Caron, S.; Heathcock, C. H. *J. Org. Chem.* **1996**, *61*, 9115–9125.
- (19) Schrag, J. D.; Li, Y.; Wu, S.; Cygler, M. *Nature* **1991**, *351*, 761–764.
- (20) Kraut, J. *Annu. Rev. Biosci.* **1977**, *46*, 331–358.
- (21) Robillard, G.; Shulman, R. G. *J. Mol. Biol.* **1972**, *71*, 507–511.
- (22) Robillard, G.; Shulman, R. G. *J. Mol. Biol.* **1974**, *86*, 541–558.
- (23) Warshel, A.; Naray-Szabo, G.; Sussman, F.; Hwang, J. K. *Biochem.* **1989**, *28*, 3629–3637.
- (24) Ishida, T.; Kato, S. *J. Am. Chem. Soc.* **2004**, *126*, 7111–7118.
- (25) Topf, M.; Varnai, P.; Richards, W. G. *J. Am. Chem. Soc.* **2002**, *124*, 14780–14788.
- (26) Blow, D. M.; Birktoft, J. J.; Hartley, B. S. *Nature* **1969**, *221*, 337–340.
- (27) Hunkapiller, M. W.; Smallcombe, S. H.; Whitaker, D. R.; Richards, J. H. *Biochem.* **1973**, *12*, 4732–4743.
- (28) Frey, P. A.; Whitt, S. A.; Tobin, J. B. *Science* **1994**, *264*, 1927–1930.
- (29) Fuhrmann, C. N.; Daugherty, M. D.; Agard, D. A. *J. Am. Chem. Soc.* **2006**, *128*, 9086–9102.
- (30) Wilmouth, R.; Edman, K.; Neutze, R.; Wright, P.; Clifton, I.; Schneider, T.; Schofield, C.; Hajdu, J. *Nat. Struct. Biol.* **2001**, *8*, 689.
- (31) Zhang, Y.; Kua, J.; McCammon, J. A. *J. Am. Chem. Soc.* **2002**, *124*, 10572–10577.
- (32) Otte, N. Ph.D. thesis, Universität Düsseldorf, Germany, 2006.
- (33) Topf, M.; Richards, W. G. *J. Am. Chem. Soc.* **2004**, *126*, 14631–14641.
- (34) Ferraboschi, P.; Casati, S.; De Grandi, S.; Grisenti, P.; Santaniello, E. *Biocatal. Biotransform.* **1994**, *10*, 279–288.
- (35) Mezzetti, A.; Keith, C.; Kazlauskas, R. J. *Tetrahedron Asym.* **2003**, *14*, 3917–3924.
- (36) Weissflock, A. N. E.; Kazlauskas, R. J. *J. Org. Chem.* **1995**, *60*, 6959–6969.
- (37) Tuomi, W. V.; Kazlauskas, R. J. *J. Org. Chem.* **1999**, *64*, 2638–2647.
- (38) Mezzetti, A.; Schrag, J. D.; Cheong, C. S.; Kazlauskas, R. J. *Chem. Biol.* **2005**, *12*, 427–437.
- (39) Tomić, S.; Dobovičnik, V.; Šunjić, V.; Kojić-Prodić, V. *Croat. Chim. Act.* **2001**, *74*, 343–357.
- (40) Tafi, A.; van Almsick, A.; Corelli, F.; Crusco, M.; Laumen, K. E.; Schneider, M. P.; Botta, M. *J. Org. Chem.* **2000**, *65*, 3659–3665.
- (41) Zuegg, J.; Höning, H.; Schrag, J. D.; Cygler, M. *J. Mol. Catal. B: Enzym.* **1997**, *3*, 83–98.
- (42) Ferraboschi, P.; Casati, S.; Manzocchi, A.; Santaniello, E. *Tetrahedron Asymm.* **1995**, *6*, 1521–1524.
- (43) Tafi, A.; Manetti, F.; Botta, M.; Casati, S.; Santaniello, E. *Tetrahedron Asymm.* **2004**, *15*, 2345–2350.
- (44) Ema, T. *Curr. Org. Chem.* **2004**, *8*, 1009–1025.
- (45) Gao, J.; Ma, S.; Major, D. T.; Nam, K.; Pu, J.; Truhlar, D. G. *Chem. Rev.* **2006**, *106*, 3188–3209.
- (46) Laio, A.; Parrinello, M. *Proc. Natl. Acad. Sci. U.S.A.* **2002**, *99*, 12562–12566.
- (47) Micheletti, C.; Laio, A.; Parrinello, M. *Phys. Rev. Lett.* **2004**, *92*, 170601.
- (48) Phillips, J. C.; Braun, R.; Wang, W.; Gumbart, J.; Tajkhorshid, E.; Villa, E.; Chipot, C.; Skeel, R. D.; Kale, L.; Schulten, K. *J. Comput. Chem.* **2005**, *26*, 1781–1802.
- (49) Humphrey, W.; Dalke, A.; Schulten, K. *J. Mol. Graph.* **1996**, *14*, 33–38.
- (50) Cornell, W. D.; Cieplak, P.; Bayly, C. I.; Gould, I. R.; Merz, K. M.; Ferguson, D. M.; Spellmeyer, D. C.; Fox, T.; Caldwell, J. W.; Kollman, P. A. *J. Am. Chem. Soc.* **1995**, *117*, 5179–5197.
- (51) Jorgensen, W. L.; Chandrasekhar, J.; Madura, J. D.; Impey, R. W.; Klein, M. L. *J. Chem. Phys.* **1983**, *79*, 926–935.
- (52) Schmidt, M. W.; Baldridge, K. K.; Boatz, J. A.; Elbert, S. T.; Gordon, M. S.; Jensen, J. H.; Koseki, S.; Matsunaga, N.; Nguyen, K. A.; Su, S. *J. Comput. Chem.* **1993**, *14*, 1347–1363.

- (53) Schrag, J. D.; Li, Y.; Cygler, M.; Lang, D.; Burgdorf, T.; Hecht, H. J.; Schmid, R.; Schomburg, D.; Rydel, T. J.; Oliver, J. D. *Structure* **1997**, *5*, 187–202.
- (54) Essmann, U.; Perera, L.; Berkowitz, M. L.; Darden, T.; Lee, H.; Pedersen, L. G. *J. Chem. Phys.* **1995**, *103*, 8577–8593.
- (55) Tuckerman, M.; Berne, B. J.; Martyna, G. J. *J. Chem. Phys.* **1992**, *97*, 1990–2001.
- (56) Grest, G. S.; Kremer, K. *Phys. Rev. A* **1986**, *33*, 3628–3631.
- (57) Feller, S. E.; Zhang, Y.; Pastor, R. W.; Brooks, B. R. *J. Chem. Phys.* **1995**, *103*, 4613–4621.
- (58) Laino, T.; Mohamed, F.; Laio, A.; Parrinello, M. *J. Chem. Theory Comput.* **2005**, *1*, 1176–1184.
- (59) Laino, T.; Mohamed, F.; Laio, A.; Parrinello, M. *J. Chem. Theory Comput.* **2006**, *2*, 1370–1378.
- (60) Lippert, G.; Hutter, J.; Parrinello, M. *Theor. Chem. Acc.* **1999**, *103*, 124–140.
- (61) VandeVondele, J.; Krack, M.; Mohamed, F.; Parrinello, M.; Chassaing, T.; Hutter, J. *Comput. Phys. Commun.* **2005**, *167*, 103–128.
- (62) The CP2K developers group. <http://cp2k.berlios.de> (accessed June 2, 2009).
- (63) Ishida, T.; Kato, S. *J. Am. Chem. Soc.* **2003**, *125*, 12035–12048.
- (64) Maseras, F.; Morokuma, K. *J. Comput. Chem.* **1995**, *16*, 1170–1179.
- (65) Schaefer, A.; Huber, C.; Ahlrichs, R. *J. Chem. Phys.* **1994**, *100*, 5829.
- (66) Goedecker, S.; Teter, M.; Hutter, J. *Phys. Rev. B* **1996**, *54*, 1703–1710.
- (67) Hartwigsen, C.; Goedecker, S.; Hutter, J. *Phys. Rev. B* **1998**, *58*, 3641.
- (68) Becke, A. D. *Phys. Rev. A* **1988**, *38*, 3098–3100.
- (69) Lee, C. T.; Yang, W. T.; Parr, R. G. *Phys. Rev. B* **1988**, *37*, 785–789.
- (70) Genovese, L.; Deutsch, T.; Neelov, A.; Goedecker, S.; Beylkin, G. *J. Chem. Phys.* **2006**, *125*, 074105.
- (71) Nosé, S. A. *J. Chem. Phys.* **1984**, *81*, 511–519.
- (72) Hoover, W. G. *Phys. Rev. A* **1985**, *31*, 1695–1697.
- (73) Laio, A.; Rodriguez-Forte, A.; Gervasio, F. L.; Ceccarelli, M.; Parrinello, M. *J. Phys. Chem. B* **2005**, *109*, 6714–6721.
- (74) Klahn, M.; Braun-Sand, S.; Rosta, E.; Warshel, A. *J. Phys. Chem. B* **2005**, *109*, 15645–15650.
- (75) Fersht, A. *Structure and Mechanism in Protein Science: A Guide to Enzyme Catalysis and Protein Folding*; W.H. Freeman and Company: New York, 1999.
- (76) Pleiss, J.; Scheib, H.; Schmid, R. D. *Biochimie* **2000**, *82*, 1043–1052.
- (77) Gentner, C.; Schmid, R. D.; Pleiss, J. *Colloids Surf., B* **2002**, *26*, 57–66.
- (78) Radisky, E. S.; Lee, J. M.; Lu, C. J. K.; Koshland, D. E., Jr. *Proc. Natl. Acad. Sci. U.S.A.* **2006**, *103*, 6835–6840.
- (79) Kim, K. K.; Hwang, K. Y.; Jeon, H. S.; Kim, S.; Sweet, R. M.; Yang, C. H.; Suh, S. W. *J. Mol. Biol.* **1992**, *227*, 1258–1262.
- (80) Kim, K. K.; Song, H. K.; Shin, D. H.; Hwang, K. Y.; Suh, S. W. *Structure* **1997**, *5*, 173–185.
- (81) Noble, M. E.; Cleasby, A.; Johnson, L. N.; Egmond, M. R.; Frenken, L. G. *FEBS Lett.* **1993**, *331*, 123–8.
- (82) Lang, D. A.; Mannesse, M. L. M.; De Haas, G. H.; Verheij, H. M.; Dijkstra, B. W. *Eur. J. Biochem.* **1998**, *254*, 333–340.
- (83) Schramm, V. L. *Arch. Biochem. Biophys.* **2005**, *433*, 13–26.
- (84) Lafaquiere, V.; Barbe, S.; Puech-Guenot, S.; Guiyssse, D.; Cortés, J.; Monsan, P.; Siméon, T.; André, I.; Remaud-Siméon, M. *ChemBioChem* **2009**, *10*, 2760–2771.

CT900636W